DYNAMICS OF BUBBLE GROWTH AND DETACHMENT FROM RIGID AND FLEXIBLE ORIFICES

Karine LOUBIERE, Gilles HEBRARD*, Pascal GUIRAUD

LIPE, Dpt G.P.I.,INSA , 135 avenue de Rangueil, 31077 Toulouse Cedex 4, France

Abstract. The objective of this paper is to understand how and why the orifice nature (rigid or flexible) governs the bubble generation. The differences in orifice nature and properties have strong consequences on the bubbles generated. Indeed, the dynamics of the formation and the nature of the detached bubbles are fundamentally different depending on whether the bubbles are generated from the rigid orifice or from the flexible orifice.
Keywords. Gas-Liquid reactors, aeration, rigid and flexible orifices, bubble formation dynamics.
Résumé. L'objectif de cette étude est de comprendre comment et pourquoi la nature de l'orifice (rigide ou flexible) contrôle la génération de bulles. Les différences de nature et de propriétés entre les deux orifices ont des conséquences notables sur les bulles générées. En effet, la dynamique de formation et la nature des bulles détachées sont fondamentalement différentes selon si elles sont générées par un orifice rigide ou par un orifice flexible. **Mots-clés.** Réacteurs Gaz-Liquide, aération, orifices rigides et flexibles, dynamiques de formation de bulles.

INTRODUCTION

A variety of chemical engineering processes are based on the use of gas-liquid reactors. The gas is released in the form of small bubbles, to yield a large surface area and also an efficient mass transfer between gas and liquid phases. Depending on the process, various gas spargers are used as aeration systems: in the chemical industries, the aeration is mainly performed with rigid nozzles (perforated plates or porous disk diffusers) whereas for waste water treatment, a gas sparger based on a flexible membrane has been developed (Loubière & Hébrard, 2003). The gas sparger plays a crucial role insofar as it has a direct influence on the hydrodynamics of the liquid and gaseous phases and so on the mass transfer (Deckwer, 1992; Hébrard et al., 1996). Indeed, the bubble size in the reactor is the outcome of the bubble formation step and of the coalescence and breakage bubble processes in the liquid medium. The present study

* Corresponding author. Tel.:00 33 05 61 55 97 89; Fax:00 33 05 61 55 97 60; E-mail address: hebrard@insa-tlse.fr

focuses on the initial step, namely on the bubble generation at the gas sparger orifices. As the field offered by this topic is wide, our research is limited to the bubble formation at a single orifice submerged in water, at rest and under atmospheric conditions; only the dynamic bubbling regime is considered. With regard to its importance and to its complexity, the bubble formation phenomenon has been the subject of many experimental and theoretical studies: two detailed reviews of the literature are given by Tsuge (1986) and Sadhal et al. (1997). However, a surprising lack of research concerning the bubble formation from a flexible orifice has been observed (Loubière, 2002); moreover, a global approach to the phenomenon (limited to the detached bubble diameter and frequency) is commonly chosen by the authors. To fill this gap, the aim of this paper is to analyse locally the dynamics of the bubble growth and detachment from a rigid orifice and from a flexible orifice, and so to understand how and why the nature of the orifice governs the bubbles generated.

EXPERIMENTAL SET-UP & METHODS

The experiments are carried out in a temperature controlled (20 °C), glass parallelepiped vessel, 0.40 m in width, 0.40 m in length and 0.50 m in height (Figure 1.(a)). The gas flow rate is regulated by a pressure gauge and by a gas flow meter. The pressure drop created by the sparger is determined using an electronic Bioblock 915PM247 type manometer. The average gas flow rate Q_G is measured using a soap film meter, through a funnel (1.5 cm diameter) put on the orifice. Air and water are used as gaseous and liquid phases (ρ_L=997 kg/m^3, μ_L=8.74.10^{-4} Pa.s, σ_L=71.8 mN/m). This set-up can be equipped with a membrane or with a rigid orifice as gas sparger.

Rigid orifice (called R.O.). One stainless steel tube is used as the rigid sparger with 12 mm external diameter and 8 mm internal diameter. The tube is perforated in order to obtain an orifice of 0.7 mm in diameter (Figure 1.(b)).

Flexible orifice (called F.O.). An industrial rubber membrane sparger is used as flexible

orifice. The bubbles are generated by a single puncture located at the membrane centre. The membrane (60 mm diameter) is assembled on a circular clamping ring composed of two jaws (Figure 1.(c)); this fixing system coupled with the use of a dynamometric spanner enables the same initial tension to be applied, thus giving reproducible results.

The dimensionless numbers characteristic of the bubble formation phenomenon, the physical characteristics of both orifices and the operating conditions are shown in Table 1. In addition, it is important to bear in mind that the particular nature of these orifices is fundamentally different. Whilst the rigid orifice is not distorted whatever the gas flow rate, the flexible orifice is punctured in a stretched rubber sheet, so its important feature is its elastic nature (Loubière & Hébrard, 2003).

Image acquisition and treatment systems. During their formation, bubbles are photographed with a Leutron LV95 camera (360 images/s). Images are visualised on the acquisition computer through the Leutron vision software. The Visilog 5.4 software performs the image treatment. The following parameters are determined: equivalent bubble diameter ($d_B \pm 12\%$), centre of gravity co-ordinates (x,y), eccentricity (χ) , contact angle ($\theta \pm 15°$) and surface/bubble contact diameter ($d_W \pm 15\%$). The bubble formation time is deduced from photographic analysis ($T_B \pm 2.78$ ms).

STUDY OF BUBBLE FORMATION FROM A RIGID ORIFICE

Thanks to image treatment, the bubble generation process can be split up into different stages and so described experimentally. Figure 2 shows typical photographs of bubble generation from the rigid orifice. The bubble generation is composed of three stages: bubble growth (Images 1-8), bubble detachment (Image 9) and bubble ascension (Images 10-18).

Analysis of the detached bubbles

Figure 3 presents the curves relating the bubble diameter at detachment and the bubble frequency to the orifice velocity. Whatever the orifice velocity, the bubble diameter at

detachment remains constant. The bubbles generated from the rigid orifice have an equivalent diameters equal to 4.5 mm; under our operating conditions, no bubble size distribution is observed. The bubble eccentricity at detachment (measured experimentally) is equal to 1.45, thus showing bubble distortions. A perfect linearity is observed between the frequency and the orifice velocity: the values of f_B remain below 30 s^{-1} in the range of the orifice velocities studied. Figure 2 shows that when the bubble detaches, no new bubble is formed in the following milliseconds: there is a time-out between two successive bubbles. The bubble formation process at the rigid orifice is also discontinuous. The bubble formation time (T_B) is the sum of a bubble growth time ($T_{B\ growth}$) and of a time-out ($T_{B\ time\text{-}out}$):

$$T_B = T_{B\ growth} + T_{B\ time\text{-}out} = 1/f_B \quad (1)$$

Described in Figure 4, the variations in T_B, $T_{B\ growth}$ and $T_{B\ time\text{-}out}$ with the orifice velocity show that the bubble formation time decreases as the orifice velocity increases, the bubble growth time remains constant (22 ms) whatever the orifice velocity, and the time-out decreases as the orifice velocity increases. For $U_{OR} < 1$ m/s, this time-out represents 90% of the bubble formation time, whereas, for $U_{OR} \cong 8$ m/s, it represents only 37% of the bubble formation time. This discontinuity of bubble formation is responsible for the low bubble frequencies measured. The presence of the time-out between two bubbles formed successively seems to be the consequence of the liquid penetration into the orifice. When a bubble detaches, the pressure in the gas chamber decreases and drops below the hydrostatic pressure, causing the liquid to penetrate into the orifice. Afterwards, the gas chamber needs a certain time to reach the minimum pressure necessary to form a new bubble: this is the time-out measured experimentally. It depends on the gas flow rate Q_G: the higher is the gas flow rate Q_G, the shorter is the time necessary to reach this pressure (Figure 4). Further experiments are necessary to confirm this phenomenon.

Dynamics of the bubble growth

As the bubble diameter and the bubble growth time do not depend on the orifice velocity, only one orifice velocity will be considered later on (the other orifice velocities give the same tendency as the chosen one).

Bubble centre of gravity and bubble radius

The bubble centre of gravity co-ordinates (x,y) and the bubble radius (R_B) are plotted versus the growth time in Figure 5.(a). It can be observed that the centre of gravity abscissa x remains nearly nil, showing that the bubble growth is symmetric about the vertical orifice axis. Moreover, two stages appear during the bubble growth. At the beginning, the centre of gravity ordinate y is slightly less than the bubble radius (t < 0.011 s), the bubble grows spherically: this is the radial expansion stage (about 30-35% of the growth time). In the second stage, the centre of gravity ordinate y becomes considerably larger than the bubble radius: this is the elongation stage (0.011 < t < 0.022 s). The bubble elongates vertically but remains attached to the orifice and a neck is formed (Figure 2, Images 7-8): when the neck of the bubble breaks off, the bubble detaches.

Bubble adhesion to the orifice surface

The hydrophobic rigid orifice surface (Table 1) has consequences on the bubble adhesion to the orifice surface. In order to shed light on this phenomenon, the surface/bubble contact diameter d_W and the bubble contact angle θ were measured experimentally. To have a better understanding of the bubble spread over the rigid orifice surface, a diagram describing this phenomenon is presented in Figure 6. The two stages previously presented appear again: the expansion stage (Figure 6.(a)), which is characterised by a decreasing contact angle and an increasing bubble spread, and the elongation stage (Figure 6.(b.1)) which is characterised by an increasing contact angle and a decreasing bubble spread.

Figures 7 show the variations in the ratio d_W/d_{OR} with the growth time. It shows that throughout the bubble growth process, the ratio d_W/d_{OR} is significantly higher than 1; thus, the

line of contact between the bubble and the surface orifice is located outside the orifice perimeter. During the radial expansion stage (t < 0.011 s), the bubble spread over the solid surface increases whereas during the elongation stage (0.011 < t < 0.022 s), it decreases. The variation in the bubble contact angle with the growth time show the same two stages (Figure 8). During the radial expansion stage (t < 0.011 s), the bubble contact angle decreases to a minimum value (about 40-50°) whereas during the elongation stage (0.011 < t < 0.022 s), it increases again. This minimum angle value could be linked to the receding contact angle of water over this particular solid surface, insofar as the contact line decreases during the bubble expansion stage (Figure 7).

Gas flow rate supplying the bubble

The gas flow rate q supplying the bubble is calculated by using the bubble volume measured experimentally:

$$q = dV_B / dt \quad (2)$$

The variation in q with the growth time is presented in Figure 9. During the radial expansion stage (t < 0.011 s), the gas flow rate q increases until it reaches about 4000 mm^3/s, whereas the elongation stage is characterised by a continuous decrease in q (0.011 < t < 0.022 s).

Moreover, it is essential to note that the instantaneous gas flow rates q supplying the bubble are significantly higher than the mean gas flow rate Q_G, due to the discontinuity of the bubble formation process at the rigid orifice as detailed previously. The high gas flow rate q does not depend on Q_G and only occurs at the orifice when the minimal pressure to form a new bubble is reached in the gas chamber.

Forces acting on the bubble during its growth. Bubble detachment.

Figure 10 shows the variation in the ratio of the experimental values of bubble volume to the theoretical Tate bubble volume with the growth time. The Tate bubble volume $V_{B\ Tate}$ (Eq.3) is usually used to predict the detached bubble volume in the static bubbling regime. It is defined by taking into account equilibrium between the buoyancy force and the surface tension force

at detachment if the bubble/surface contact angle is equal to 90° (perfect wettability):

$$V_{B\_Tate} = \frac{\pi . d_W . \sigma_L}{(\rho_L - \rho_G).g} \quad (3)$$

As shown in Figure 10, the bubble continues to grow even though the Tate volume has been reached. According to Georgescu (1999), the Tate volume accurately predicts the detached bubble volume only for *Eö* > 0.1 and *We* << 1. Under our conditions, even though *Eö* = 0.1 (Table 1), the Weber numbers are around 1000 if they are calculated using the true gas flow rate *q* instead of Q_G. Thus, liquid inertia would account for the Tate Volume underestimating the bubble volume. In order to confirm this hypothesis, the vertical components of the several forces acting on the bubble were determined using the experimental data. The following expressions are taken from previous literature (Tsuge, 1986; Loubière, 2002); they are certainly not perfect for a non-spherical growing bubble in contact with a wall, but no more precise information is available in the literature, so they were taken by default. The used forces are expressed as:

- The buoyancy force F_B: $F_B = (\rho_L - \rho_G).g.V_B$ (4)

- The force related to the gas momentum through the orifice F_M: $F_M = \frac{4.\rho_G.q^2}{\pi.d_{OR}^2}$ (5)

- The surface tension force F_S (Klausner et al., 1993): $F_S = -\pi.d_W.\sigma_L.\sin(\theta)$ (6)

- The viscous drag force F_D: $F_D = -0.125.\rho_L.\pi d_B^2.C_D.(dy/dt)^2$ (7)

  C_D is calculated using the Schiller & Nauman correlation (1935).

- The added mass force F_I (Milne-Thomson, 1955): $F_I = -\frac{d}{dt}\left(\frac{11}{16}.\rho_L.V_B.\frac{dy}{dt}\right)$ (8)

The variations in these forces with the growth time are plotted in Figure 11.(a). The viscous drag force and the gas momentum force remain negligible throughout the bubble growth (about 10^{-7}-10^{-6} N); in contrast, the buoyancy force, the surface tension force and the added mass force (about 10^{-4} N) are the determining forces. The variation in the surface tension

force with the growth time is characterised by the presence of a maximum, corresponding to the moment of the maximal bubble spreading over the orifice surface (Figure 7).

The added mass force behaves in a special way. At the beginning of the bubble growth, the bubble vertical expansion is retarded because of the high liquid inertia; then, the added mass force decreases and falls to a minimum value (around 0.015 s): thus, the bubble remains attached to the orifice thanks to the surface tension force. Afterwards, the added mass force increases again and finally decreases near the detachment. At detachment, the buoyancy force is maximal and the added mass force minimal. Such behaviour then raises the question of why the bubble does not detach at 0.015 s as the added mass force is minimal and as the Tate volume is reached. In order to answer this question, it is essential to relate this curve to the previous ones. Indeed, at 0.01 s, the gas flow rate q supplying the bubble decreases (Figure 9); thus, the bubble is slowed down in its ascension; the bubble vertical velocity $\mathrm{d}y/\mathrm{d}t$ decreases continuously until levelling off at 0.015 s: at this moment, the liquid inertia is overcome. Then, the buoyancy force enables the bubble to elongate (neck formation, Figure 2): $\mathrm{d}y/\mathrm{d}t$ increases slightly, which gives the liquid inertia to rise again. Coupled with the surface tension force, the inertial force intensifies the bubble retardation. Consequently, instead of detaching, the bubble grows again: the detachment is delayed to 0.022 s.

Before closing this paragraph, another point has to be mentioned. In the view of the literature (Georgescu, 1999), the profiles of bubble diameter and frequency obtained (Figure 3) are characteristic of the static bubbling regime, but the high liquid inertia (Figure 11.(a)) invalidates this idea. In fact, our operating conditions correspond closely to the dynamic bubbling regime and not to the static regime. This remark proves that it would be rash to define a bubbling regime by only taking into account the bubble diameter and frequency curves as a function of the orifice velocity.

Bubble ascension after detachment

As shown in Figure 2, after its detachment, the bubble is really distorted (spherical cap) by the effects of the liquid inertia and surface tension. The bubble trajectory during its ascension is not a straight line, but seems to be either in zigzag or helicoidal (Clift et al., 1978). Figure 12.(a) shows the variation in the vertical bubble velocity with time after bubble detachment. As the bubble goes up, the vertical bubble velocity shows an overall increase and does not stabilise at its terminal velocity within the study height (3 cm); Grace & Wairegi (1986) have shown that depending on the water purity, the bubble terminal velocity for d_B = 4.5 mm varies between 18 and 30 cm/s. Moreover, this variation in velocity is oscillating and quasi-periodic in nature: the experimental period values vary between 20 and 28 ms. For large bubble distortions, this phenomenon can be associated with shape oscillations. Lamb (1945) defines a time τ characteristic of the shape oscillations, as a function of the liquid properties:

$$\tau = (\rho^* . d_B^3 / \sigma_L)^{0.5} \quad (9)$$

This expression does not take into account the viscous effects of the liquid phase, but only the effects of the liquid inertia through a modified liquid density ($\rho^* = \rho_G + 0.5.\rho_L$). For bubbles of 4.5 mm in diameter, the calculated time τ of 25 ms lies within the experimentally determined range.

STUDY OF BUBBLE FORMATION FROM A FLEXIBLE ORIFICE

Figure 13 shows typical photographs of bubble generation from the flexible orifice. As with the rigid orifice, the bubble generation is composed of three stages: bubble growth (Images 1-9), bubble detachment (Image 10) and bubble ascension (Images 11-18).

Analysis of the detached bubbles

Figure 3 presents the curves relating the bubble diameter at detachment and the bubble frequency to the orifice velocity. Unlike the case of the rigid orifice, the bubble diameter increases logarithmically with the orifice velocity. Such a behaviour is specific to membrane spargers (Hebrard et al., 1996; Loubière & Hebrard, 2003); this profile correlates to the orifice

opening as increasing gas flow rate is applied. For a given orifice velocity, the bubbles generated from the flexible orifice (d_B < 2.5 mm) are noticeably smaller than the bubbles generated from the rigid orifice ($d_B \cong$ 4.5 mm). No size distribution is observed whatever the orifice velocity. The bubbles formed are virtually spherical (χ = 1.2), unlike those generated from the rigid orifice. With regard to the bubble frequency, a specific behaviour is observed (Figure 3). For U_{OR} < 2.5 m/s, the bubble frequency increases linearly with the orifice velocity; for U_{OR} > 2.5 m/s, f_B levels off and remains almost constant, around 77 s^{-1}. For a given orifice velocity, the bubble frequencies obtained with the flexible orifice are significantly higher than those obtained for the rigid orifice. As shown in Figure 13, no time-out exists between two bubbles formed successively at the flexible orifice: at the moment when a bubble detaches, a new bubble grows, pushing off the previous one. This means that the bubble formation time is also equal to the bubble growth time ($T_B = T_{B\_growth}$). For a given gas flow rate Q_G, the pressure in the gas chamber remains constant (no fluctuation was detected experimentally) and is high enough to prevent the liquid from penetrating into the orifice: the bubble formation is thus continuous and dependent on the gas flow rate Q_G.

Dynamics of the bubble growth

Bubble centre of gravity and bubble radius

Figure 5.(b) illustrates an example of the bubble centre of gravity co-ordinates (x, y) and radius (R_B) curves versus growth time. As with the rigid orifice, whatever the orifice velocity, the bubble growth remains symmetric about the vertical orifice axis and is composed of two stages: a radial expansion stage (t < 0.0139 s) and an elongation stage (t > 0.0139 s). Nevertheless, in the case of bubbles generated from the flexible orifice, the radial expansion stage is longer and depends on the orifice velocity: some experiments (Loubière, 2002) have shown that for low U_{OR}, it can represent about 70% of the growth time.

Bubble adhesion to the orifice surface

The flexible orifice surface is hydrophobic (Table 1). As with the rigid orifice, the surface/bubble contact diameter d_W and the bubble contact angle θ were measured experimentally. To analyse the bubble spread over the flexible orifice surface, a diagram describing this phenomenon is presented in Figure 6. As with the rigid orifice, the bubble spreading phenomenon is composed of two stages. The expansion stage (Figure 6. (a)) has the same characteristics as those of the rigid orifice, but the elongation stage (Figure 6.(b.2)) is different: a decreasing contact angle and a decreasing bubble spread are observed.

Figures 7 show the variations in the ratio d_W/d_{OR} with the growth time. It shows that d_W/d_{OR} remains roughly above 1: the bubble also spreads over the surface. The curves relating the d_W/d_{OR} ratio and the growth time have the same shape than those with the rigid orifice; nevertheless, some differences do appear: the two characteristic stages (increasing spreading and decreasing spreading) are less pronounced than in the case of the rigid orifice, and an increasing orifice velocity tends to intensify the bubble spreading. The variation of the bubble contact angle with the growth time is presented in Figure 8. Unlike the case of the rigid orifice, the bubble contact angle decreases throughout the bubble growth. The orifice velocity has no influence within the limits of experimental error (± 15°).

Gas flow rate supplying the bubble

The curves relating q (Eq.(2)) to the growth time are plotted in Figure 9. Whatever the orifice velocity, the gas flow rate q supplying the bubble remains almost constant during the bubble growth, and is equal to Q_G. This result is the consequence of the bubble formation continuity at the flexible orifice: the pressure in the gas chamber is high enough to enable q to remain constant during the bubble growth. A higher gas flow rate Q_G gives a higher pressure in the gas chamber and a higher q: thus, the bubbles generated depend on Q_G (Figure 3).

Forces acting on the bubble during its growth. Bubble detachment.

Figure 14 presents the variation in the ratio of the experimental value of bubble volume at

detachment to the theoretical Tate volume (Eq.3) with the Froude number. The Froude number is used to plot several gas flow rates Q_G, taking into account the variation in d_{OR} with Q_G. Contrary to the rigid orifice, the flexible orifice generates bubbles detaching before the Tate volume is reached, whatever the operating conditions. According to Georgescu (1999), the "premature" bubble detachment is linked to low Eötvos numbers, which are around 0.01 with the flexible orifice (Table 1). Due to the small orifice diameter, the instability sequence responsible for the neck formation is longer and more pronounced, the neck pinching thus occurs earlier. As with the rigid orifice, the vertical components of the several forces acting on the bubbles generated from the flexible orifice were calculated. Figure 11.(b) illustrates typical curves obtained for bubbles generated from the flexible orifice. Viscous drag, gas momentum and added mass forces are negligible throughout the bubble growth (10^{-8}-10^{-7} N). In contrast, the buoyancy and the surface tension forces are determinant (10^{-4}-10^{-5} N). As with the rigid orifice, the surface tension force curve has a parabolic shape (Figure 11.(a)). Unlike the case of the rigid orifice, the added mass force is negligible, mainly due to the low gas flow rate q supplying the bubble (Figure 9). The bubble detachment occurs when the buoyancy force is maximal and the surface tension force minimal, but before reaching the Tate volume.

Bubble ascension after detachment

As shown in Figure 13, after detachment, the bubble remains for several milliseconds (around 0.011 s) "stuck" near the next growing bubble, and is also slightly distorted by the effects of the next bubble growth and elongation. After 0.0417 s, the bubble really begins its ascension, keeping its spherical shape; its trajectory seems to be almost a straight line. Figure 12.(b) shows the variation in the vertical bubble velocity with time after bubble detachment. Whatever the orifice velocity, the vertical bubble velocity increases continuously until levelling off; afterwards, the vertical bubble velocity remains constant at around 0.3 m/s, corresponding to its terminal velocity: this value is confirmed by Grace & Wairegi (1986).

CONCLUSION

This research has shown that the differences in orifice nature and properties have a strong impact on the associated bubble formation phenomena:

- For a given gas flow rate Q_G, the bubbles formed at the rigid orifice have significantly larger sizes and lower formation frequencies than the bubbles formed at the flexible orifice.
- For the rigid orifice, the detached bubble diameter and growth time do not depend on the gas flow rate Q_G whereas for the flexible orifice, the bubble diameter and frequency increase with Q_G.

These local analyses (bubble formation dynamics) demonstrate that:

- For the rigid orifice, the bubbles are controlled not by the gas flow rate Q_G, but by the minimum pressure in the gas chamber required to form a new bubble. When this pressure is reached, the instantaneous gas flow rate q supplying the future bubble is generated through the orifice, is always the same, independent of the operating condition.
- For the flexible orifice, the pressure in the gas chamber is sufficiently high to prevent the liquid from penetrating into the orifice (no time-out) and to enable the gas flow rate q supplying the bubble to be constant during the bubble growth.

In a full scale gas-liquid reactor, these different bubble generations would have a strong impact on the gas hold-up, on the interfacial area and on the mass transfer. The impact of surfactant molecules present the liquid medium on the bubbles would also not be the same, depending on whether the bubbles are generated from the rigid orifice or from the flexible orifice (Loubière et al., 2002).

Nomenclature

C_D	= Drag coefficient	[-]	g	= Acceleration due to gravity	[m/s^2]
C_I	= Added mass coefficient	[-]	H_L	= Liquid height	[m]
d_{OR}	= Equivalent orifice diameter	[m]	Q_G	= Mean gas flow rate (measured with the	
d_W	= Surface/bubble contact diameter	[m]		soap film meter)	[m^3/s]
f_B	= Bubble frequency	[s^{-1}]	p_H	= Hydrostatic pressure	[Pa]

ΔP_C = Critical pressure (minimal pressure required to initiate the bubbling) [Pa]

U_{OR} = Orifice velocity defined as $U_{OR} = Q_G / (\pi . d_{OR}^2 / 4)$ [m/s]

T_B = Bubble formation time [s]

V_B = Bubble volume [m^3]

V_C = Gas chamber volume between the control valve and the orifice [m^3]

Greek symbols

γ_C = Wetting critical surface tension of the orifice surface [N/m]

θ = Contact angle between the bubble and the orifice surface [°]

μ_G = Gas viscosity [Pa.s]

μ_L = Liquid viscosity [Pa.s]

ρ_G = Gas density [kg/m^3]

ρ_L = Liquid density [kg/m^3]

σ_L = Liquid surface tension [N/m]

χ = Bubble eccentricity [-]

Dimensionless Number

Eö = Eötvos number defined as $Eö = \rho_L . d_{OR}^2 . g / \sigma_L$ [-]

Fr = Froude number defined as $Fr = U_{OR}^2 / (d_{OR} . g)$ [-]

N_C = Capacitance number defined as $N_C = 4 . V_C . \rho_L . g / (\pi . d_{OR}^2 . p_H)$ [-]

N_W = Gas flow rate number defined as $N_W = Eö . Fr^{0.5}$ [-]

Re_{OR} = Orifice Reynolds number defined as $Re_{OR} = \rho_G . U_{OR} . d_{OR} / \mu_G$ [-]

We = Weber number defined as $We = \rho_L . U_{OR}^2 . d_{OR} / \sigma_L$ [-]

References

Clift R., Grace J.R., Weber M.E., “Bubbles, drops and particles”, Academic press (1978).

Deckwer W.D., “Bubble column reactors”, John Wiley & Sons Ltd, England, (1992).

Georgescu S.C., “Evolution d’une bulle : Formation à partir d’un orifice rigide et Eclatement à la traversée d’une surface libre”, Thesis, INP Grenoble et Université Politechnica de Bucarest, France (1999).

Grace J.R., & Wairegi T., “Properties and Characteristics of drops and bubbles”, in “Encyclopedia of Fluid Mechanics”, Cheremisinoff, Chap. 3, Gulf Publishing Corporation, Houston, TX, (1986), pp. 43-57.

Hébrard G., Bastoul D., & Roustan M., “Influence of the gas sparger on the hydrodynamic behaviour of bubble columns”, Trans IchemE, **74**, A, 406-414, (1996).

Klausner J.F., Mei R., Bernhard D.M., & Zeng L.Z., “Vapor bubble departure in forced convection boiling”, Int. J. Heat Mass Transfer, **36**, 3, 651-662, (1993).

Lamb H., “Hydrodynamics”, Dover, New-York (1945).

Loubière K., “Croissance et Détachement de bulles générées par des orifices rigides et flexibles dans des phases liquides newtoniennes: Etude expérimentale et Modélisation”, Thesis N°663, INSAT, France, (2002).

Loubière K. & Hébrard G., “Bubble formation from a flexible hole submerged in an inviscid liquids”, Chem. Eng. Sc., **58**, 135-148 (2003).

Loubière K., Moustiri S., Hébrard G., Seidlitz F., “Bubble formation model for rigid and flexible orifices submerged in inviscid liquids”, dans “Proc. ISCRE 17”, Hong-Kong, August 25-28 (2002).

Milne-Thomson L.N., “Theoretical Hydrodynamics”, London : MacMillan & Co Ltd., 3rd edition, (1955).

Sadhal S.S., Ayyaswany P.S., & Chuang J.N., “Transport Phenomena with Drops and Bubbles”, Springer Verlag NY Inc, Chapitre 7, (1997), pp. 311-402.

Schiller L., Nauman A., “A drag coefficient correlation”, V.D.I. Zeitung, **77**, 318-320, (1935).

Tsuge H., “Hydrodynamics of bubble formation from submerged orifice”, in “Encyclopedia of Fluid Mechanics”, Cheremisinoff, Chap. 9, Gulf Publishing Corporation, Houston, TX, (1986), pp. 191-232.

Table legend

Table 1. Bubble formation dimensionless numbers, physical characteristics of the rigid and flexible orifices and operating conditions. [(1) These dimensionless numbers are calculated using the mean orifice velocity U_{OR} (deduced from Q_G). (2) The membrane bulging is not included. (3) Measured under a liquid height H_L. (4) Measured by using a camera coupled with a microscope, the equivalent orifice diameters used correspond to the diameter of circular hole with the same area (Loubière & Hébrard, 2003)]

Figure Legend

Figure 1 Experimental set-up
(a) Diagram [1. Pressure gauge, 2. Gas flow meter, 3. Electronic manometer, 4. Glass vessel, 5. Gas sparger orifice, 6. Funnel, 7. Soap film meter, 8. Temperature controlled]. (b) Rigid orifice. (c) Fixing system of the flexible membrane; expanding orifice photographs.

Figure 2 Bubble formation photographs for bubbles generated from the rigid orifice (U_{OR}=0.56 m/s).

Figure 3 Bubble diameter and frequency versus orifice velocity for bubbles generated from the rigid orifice (Filled symbols) and from the flexible orifice (Not-filled symbols).

Figure 4 Bubble formation time, bubble growth time and time-out versus orifice velocity for bubbles generated from the rigid orifice (U_{OR}=0.56 m/s).

Figure 5 Bubble radius, co-ordinates of bubble centre of gravity versus growth time
(a) Rigid orifice (U_{OR}=0.56 m/s). (b) Flexible orifice (U_{OR}=1.03 m/s)

Figure 6 Diagram of the bubble spread over the rigid and the flexible orifice surface. (a) Radial expansion stage. (b) Elongation stage.

Figure 7 Ratio of the surface/bubble contact diameter to the orifice diameter versus growth time (Filled symbol: Rigid orifice; Not-filled symbol: Flexible orifice)

Figure 8 Bubble contact angle versus growth time (Filled symbol: Rigid orifice; Not-filled symbol: Flexible orifice)

Figure 9 Gas flow rate q supplying the bubble versus growth time (Filled symbol: Rigid orifice; Not-filled symbol: Flexible orifice)

Figure 10 Ratio of the experimental bubble volume to the theoretical Tate volume versus growth time (Rigid orifice, U_{OR}=0.56 m/s)

Figure 11 Vertical components of the different forces acting on the bubble during its growth
(a) Rigid orifice (U_{OR}=0.56 m/s). (b) Flexible orifice (U_{OR}=0.51 m/s).

Figure 12 Vertical bubble velocity versus time after bubble detachment
(a) Rigid orifice (U_{OR}=0.56 m/s). (b) Flexible orifice.

Figure 13 Bubble formation photographs for bubbles generated from the flexible orifice (U_{OR}=1.03 m/s)

Figure 14 Ratio of the experimental value of bubble volume at detachment to the theoretical Tate volume versus Froude number (flexible orifice)

Table 1

Characteristic parameters	**Rigid Orifice (R.O.)**	**Flexible Orifice (F.O.)**
$\boldsymbol{N_C}$ (1)	8	70 - 160
$\boldsymbol{N_W}$ (1)	0.5 - 6	0.04 - 7
$\boldsymbol{We}$ (1)	4.10^{-3} - 0.8	2.10^{-4} - 2
$\boldsymbol{Re_{OR}}$ (1)	28 - 393	4 - 500
$\boldsymbol{Eö}$ (1)	0.1	0.01 – 0.03
Thickness (mm)	2.00	2.15
$\boldsymbol{V_C}$ (2) (cm^3)	33.4	101
$\boldsymbol{\gamma_C}$ (mN/m)	19	23
$\boldsymbol{\Delta P_C}$ (3) (mbars)	32	115
$\boldsymbol{H_L}$ (m)	0.33	0.20
$\boldsymbol{d_{OR}}$ (4) (mm)	0.7	0.29 - 0.45
$\boldsymbol{U_{OR}}$ (m/s)	0.56 - 7.8	0.17 - 16

Figure 1

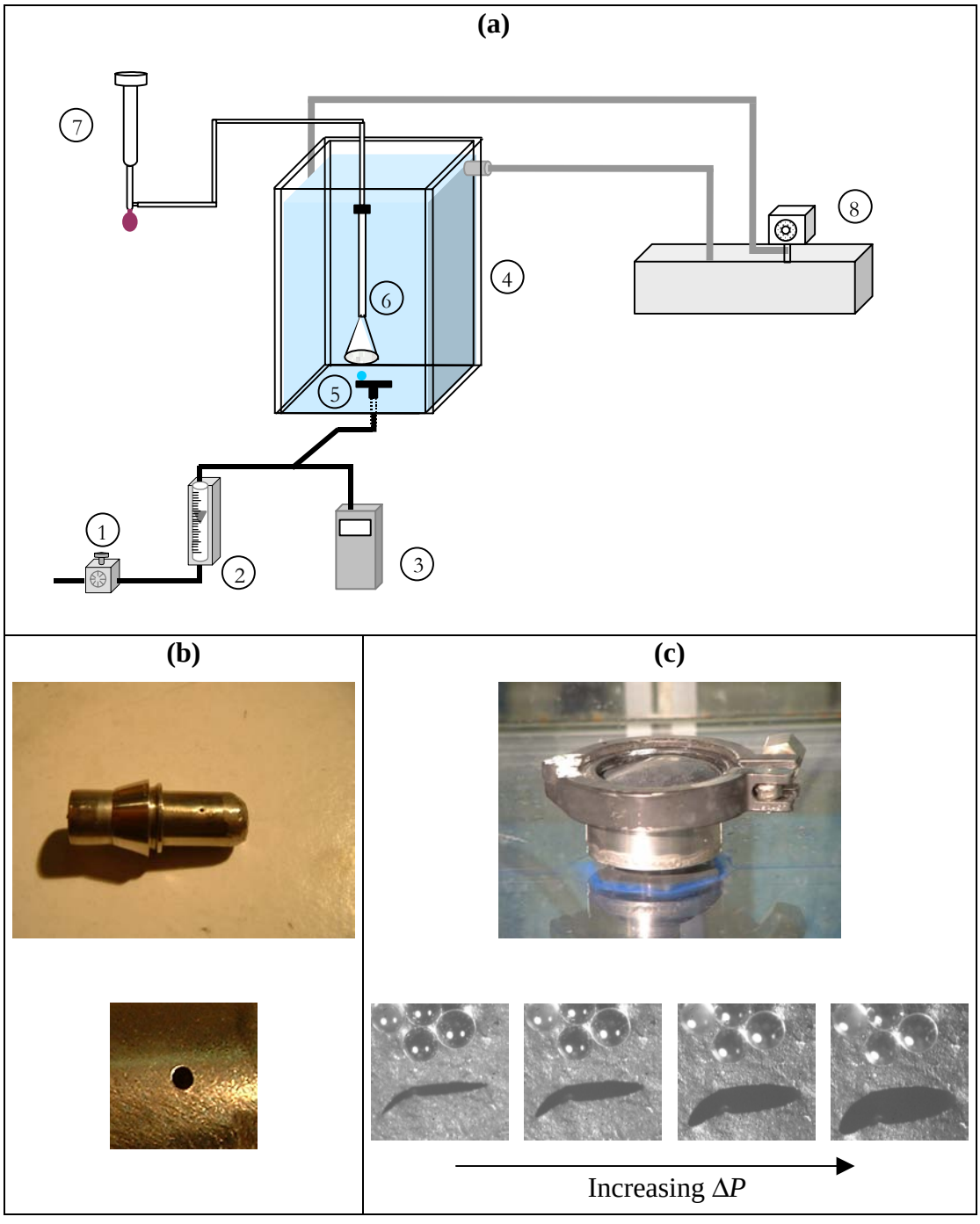

Figure 2

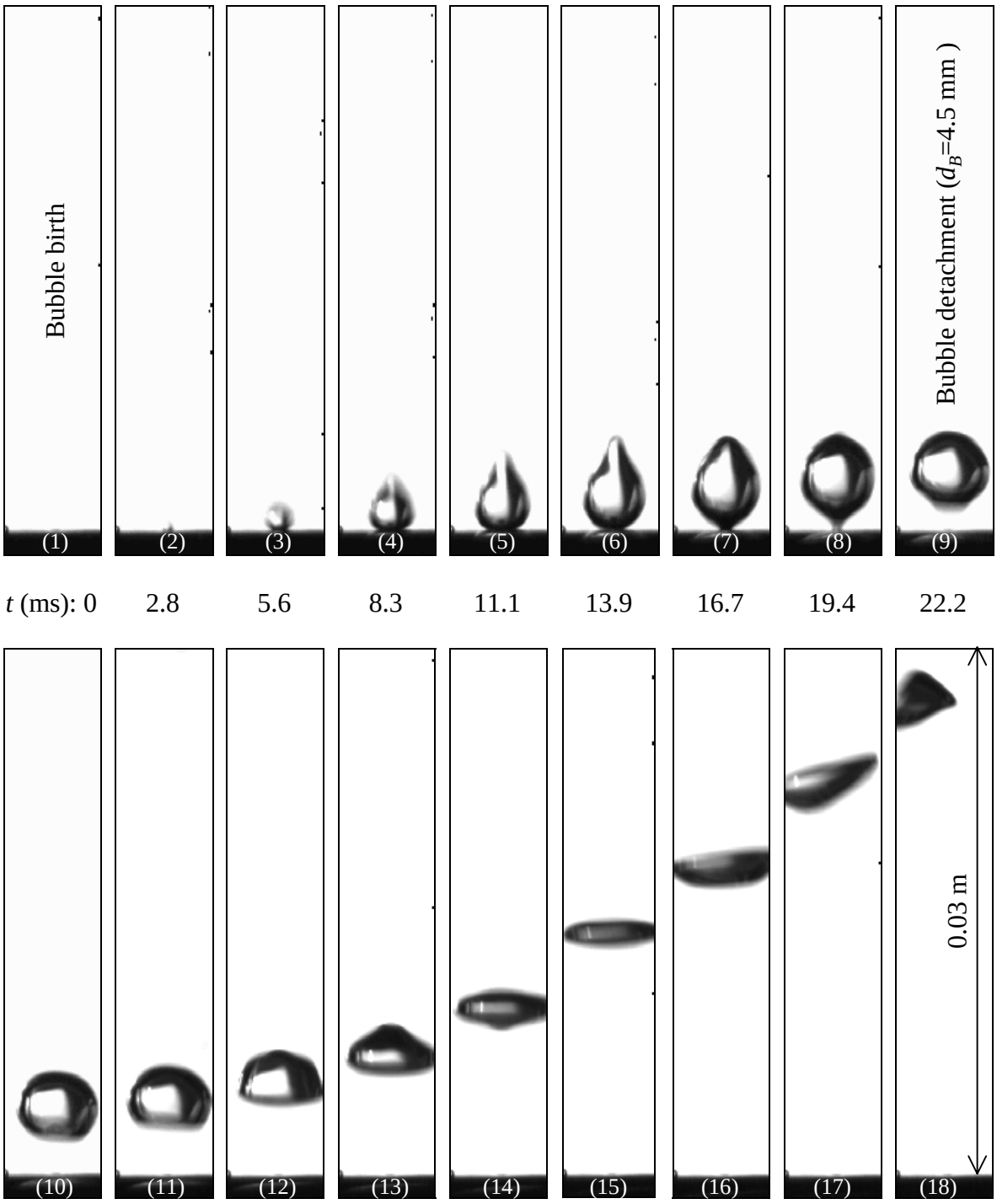
Bubble birth
Bubble detachment (d_B=4.5 mm)
(1)
(2)
(3)
(4)
(5)
(6)
(7)
(8)
(9)
t (ms): 0
2.8
5.6
8.3
11.1
13.9
16.7
19.4
22.2
0.03 m
(10)
(11)
(12)
(13)
(14)
(15)
(16)
(17)
(18)
25
27.8
33.3
41.7
55.6
75
91.7
111.1
130.6

Figure 3

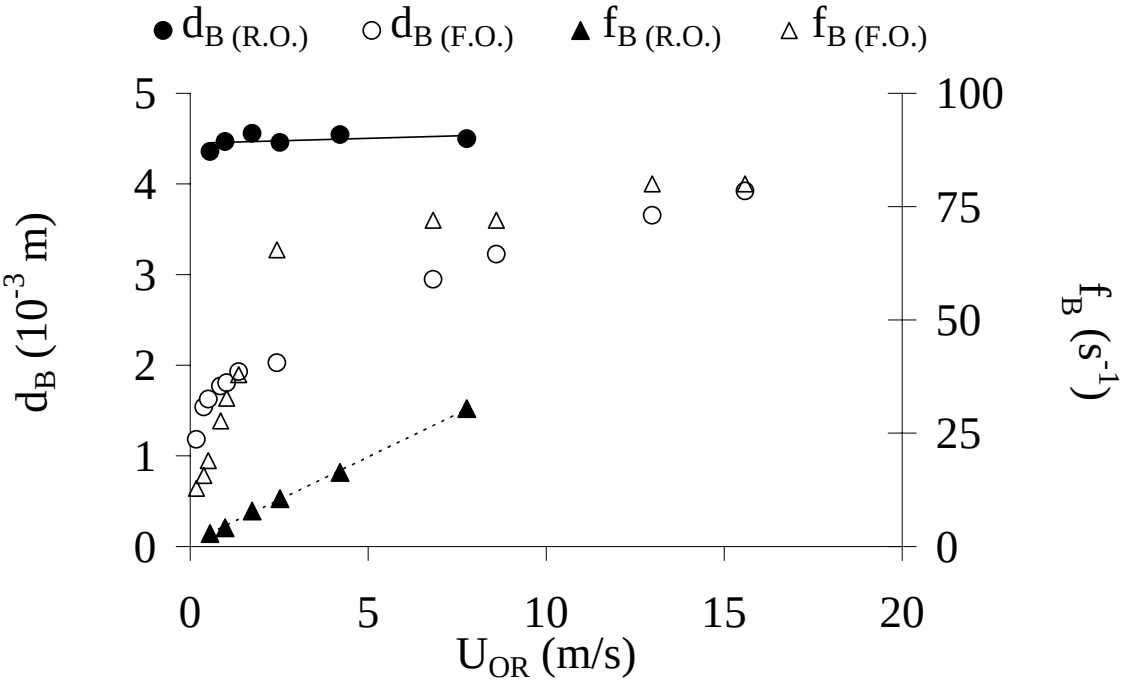

Figure 4

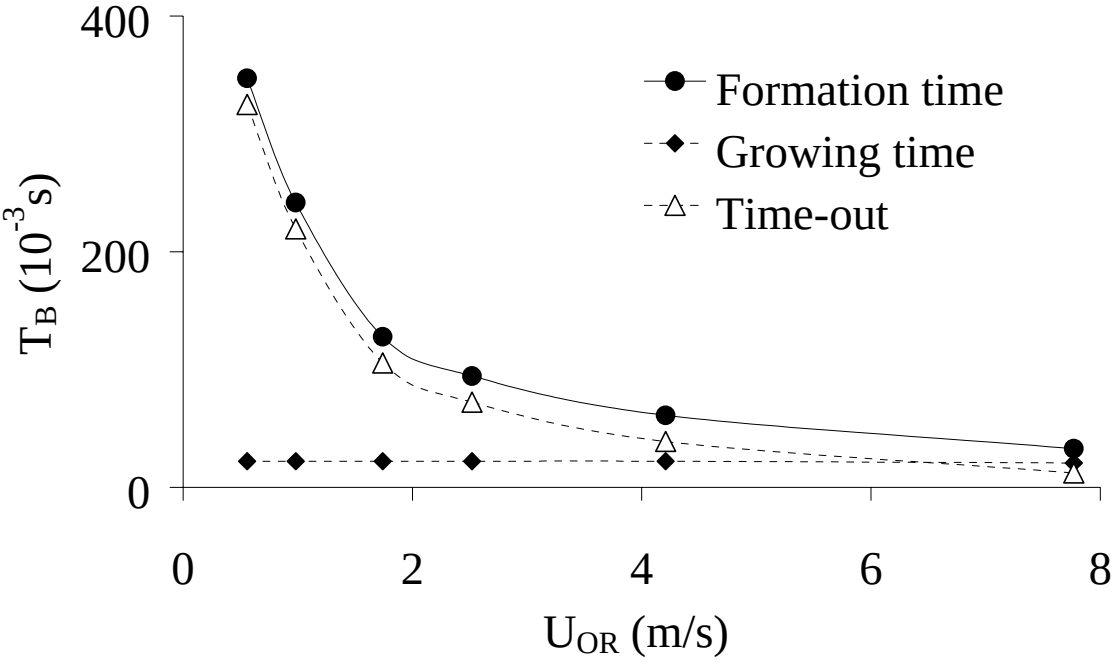

Figure 5

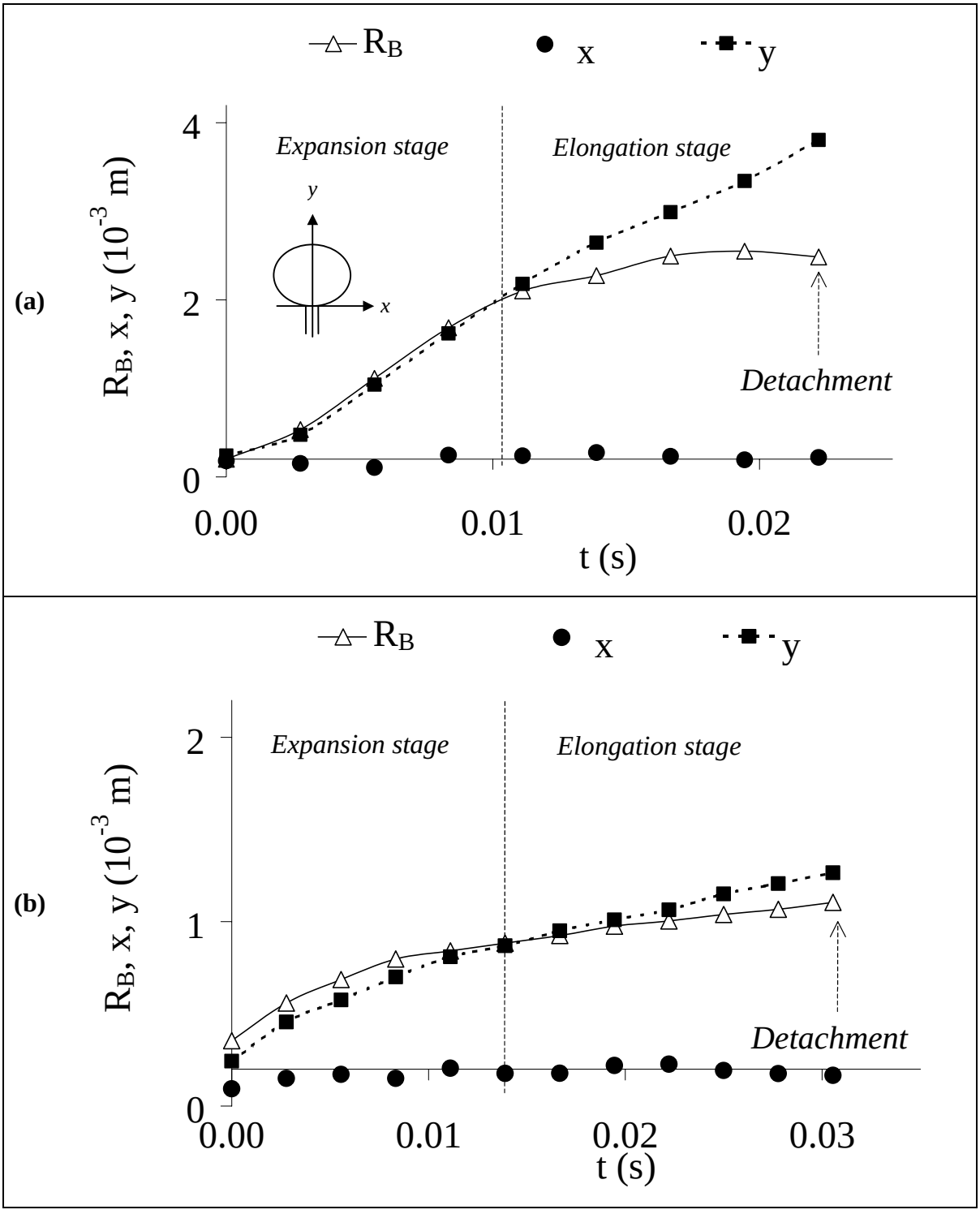
(a)
R_B
x
y
Expansion stage
Elongation stage
y
x
Detachment
R_B, x, y (10^-3 m)
4
2
0
0.00
0.01
0.02
t (s)
(b)
R_B
x
y
Expansion stage
Elongation stage
Detachment
R_B, x, y (10^-3 m)
2
1
0
0.00
0.01
0.02
0.03
t (s)

Figure 6

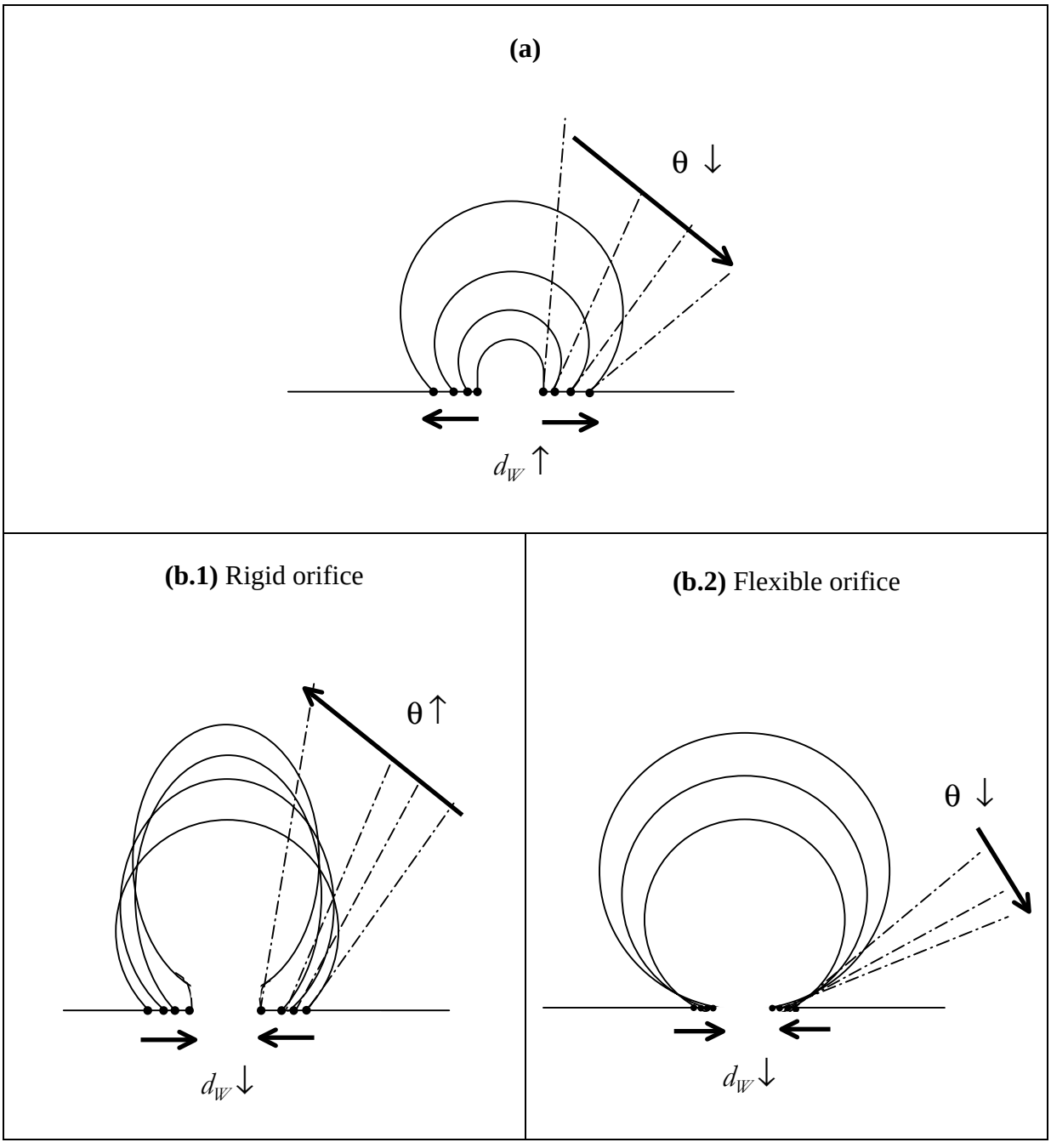

Figure 7

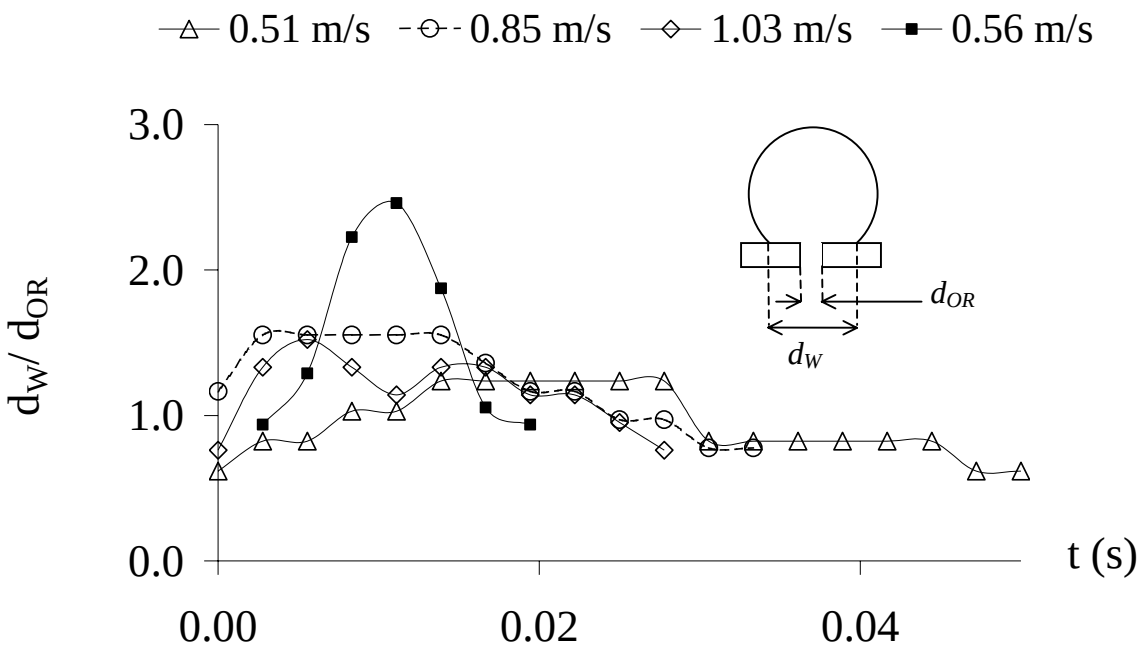

Figure 8

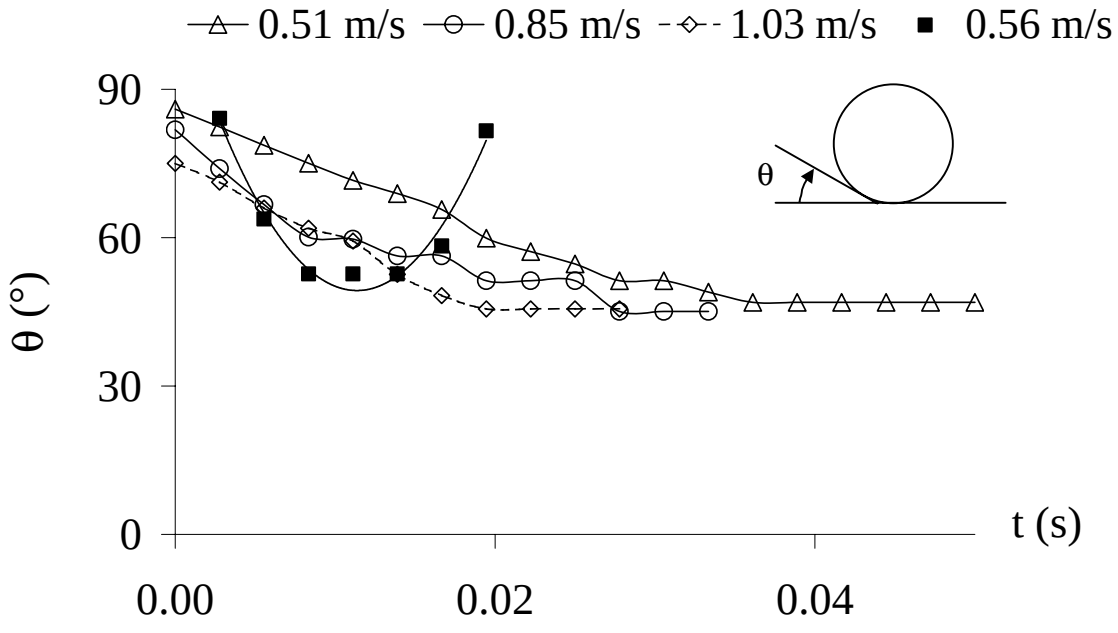

Figure 9

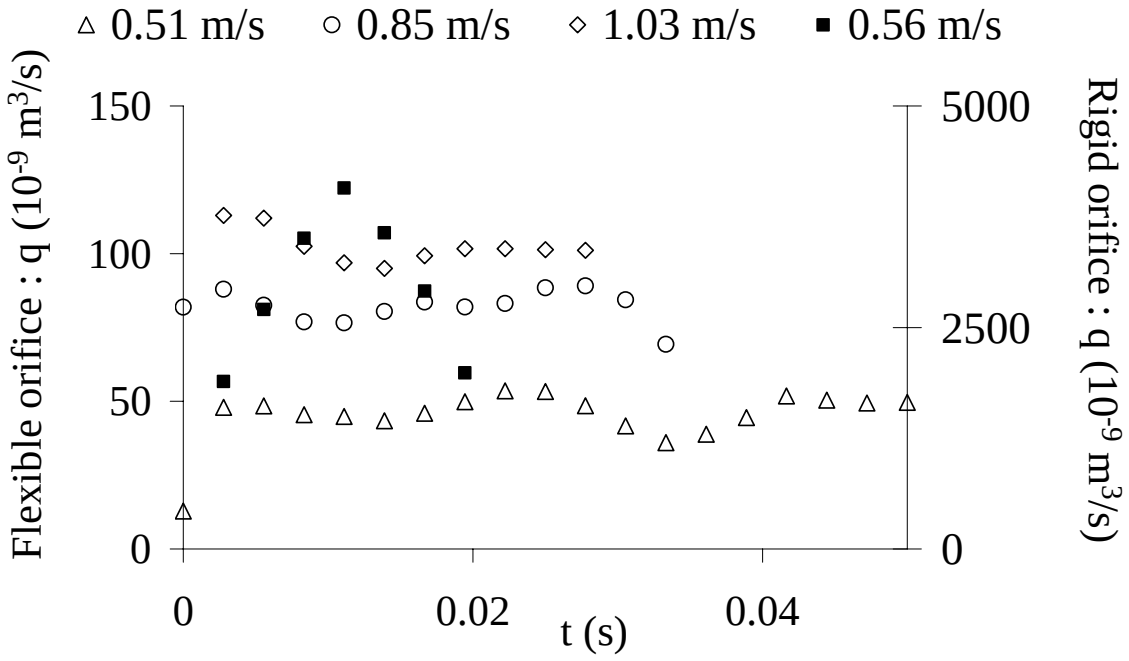

Figure 10

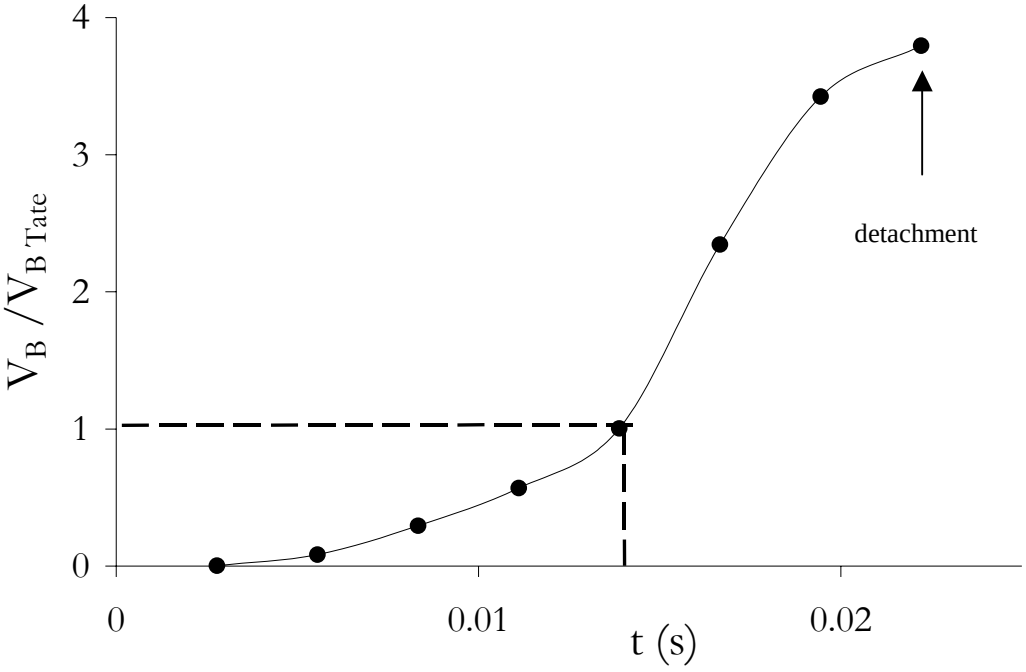

Figure 11

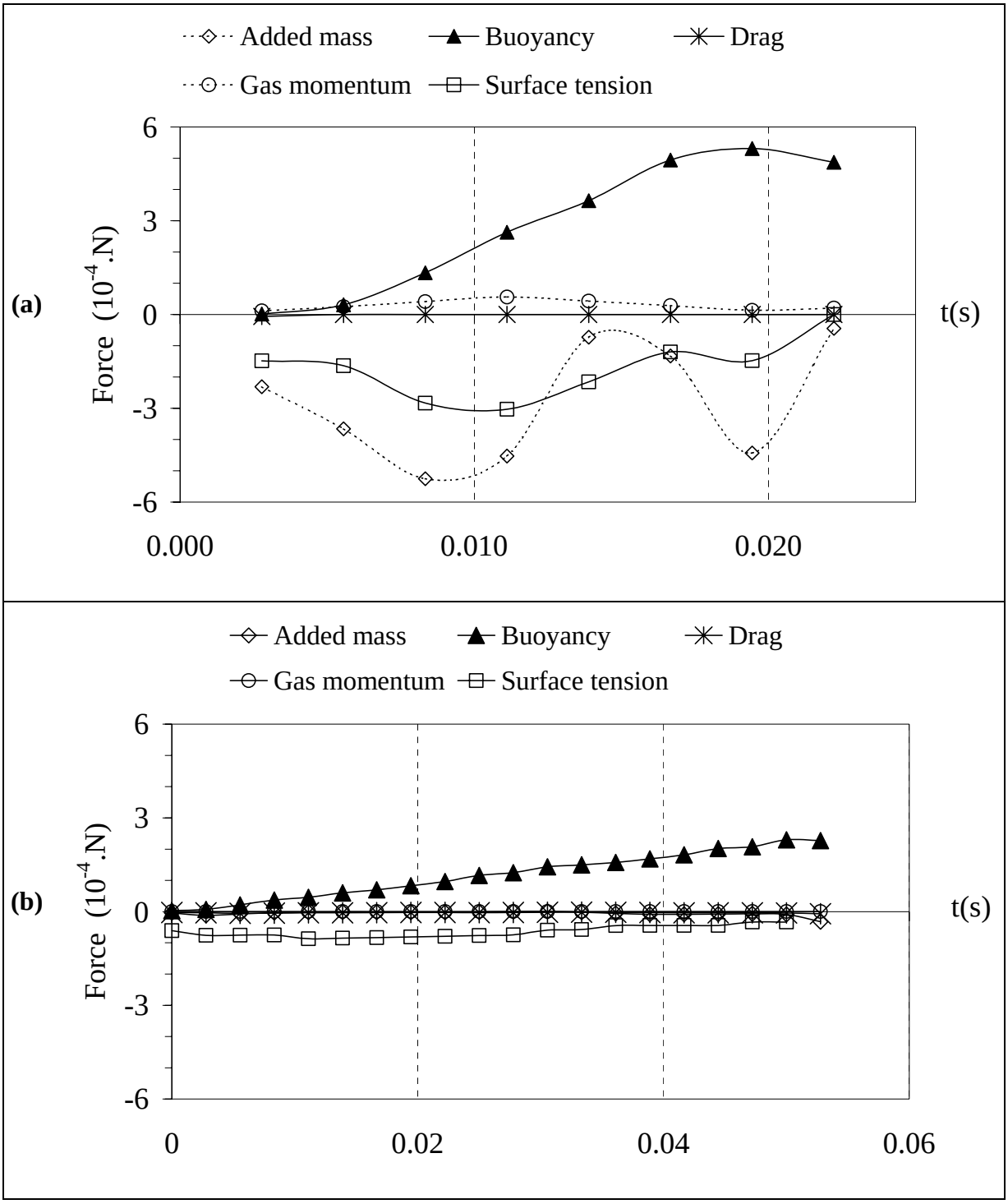
Added mass
Buoyancy
Drag
Gas momentum
Surface tension
(a)
Force (10-4.N)
6
3
0
-3
-6
0.000
0.010
0.020
t(s)
(b)
Force (10-4.N)
6
3
0
-3
-6
0
0.02
0.04
0.06
t(s)

Figure 12

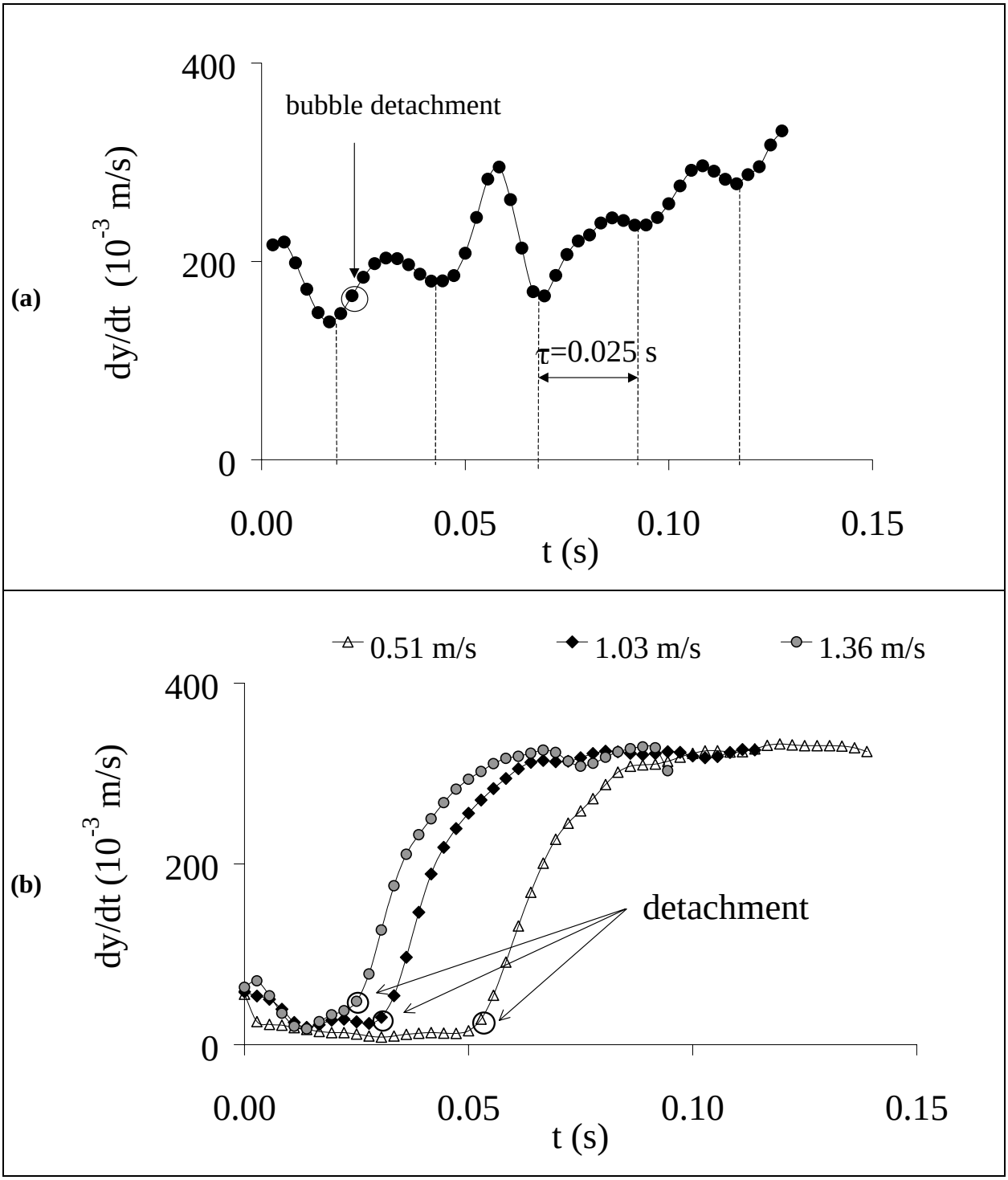
(a)
400
200
0
bubble detachment
τ=0.025 s
dy/dt (10-3 m/s)
0.00
0.05
0.10
0.15
t (s)
(b)
0.51 m/s
1.03 m/s
1.36 m/s
400
200
0
detachment
dy/dt (10-3 m/s)
0.00
0.05
0.10
0.15
t (s)

Figure 13

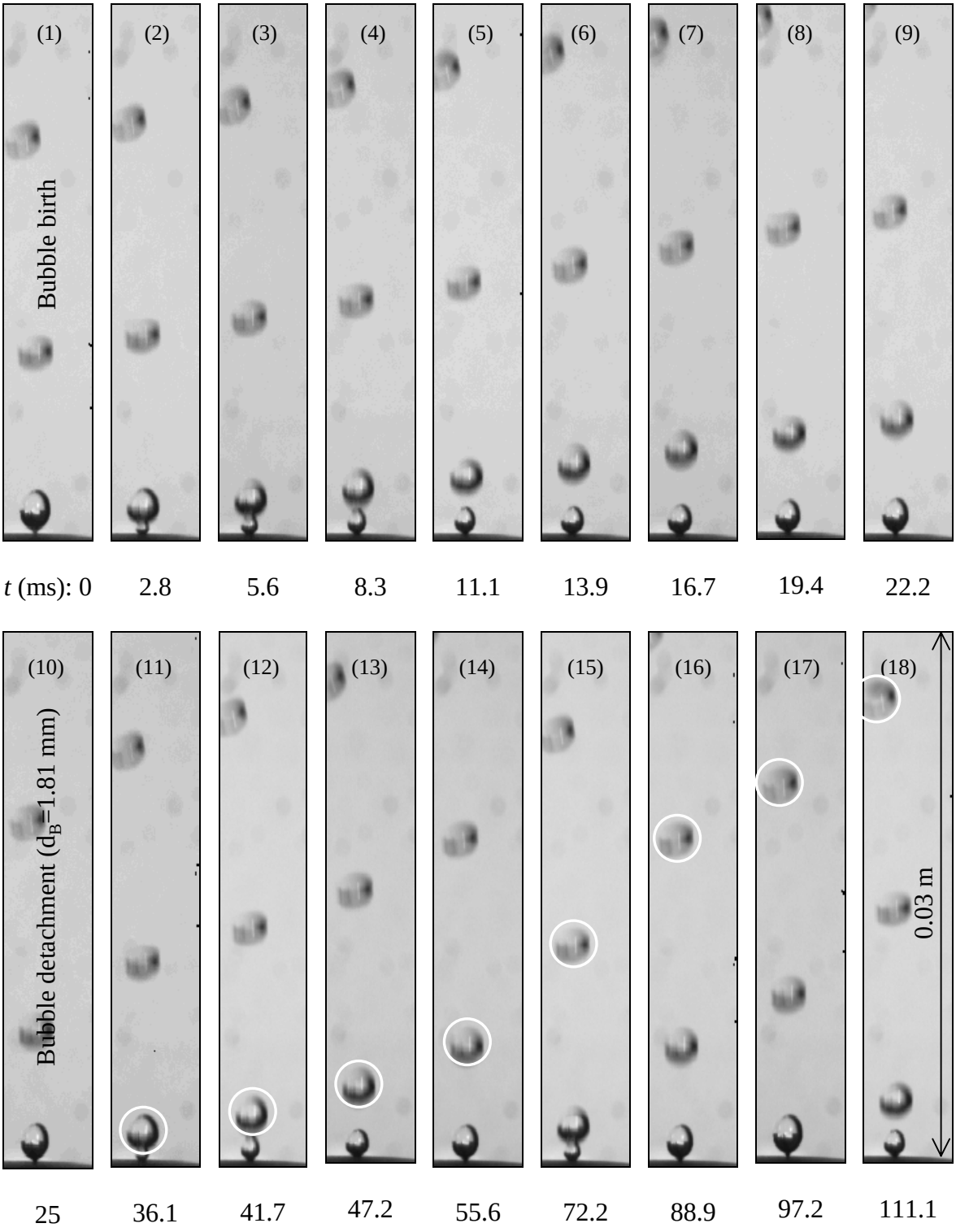
(1)
Bubble birth
(2)
(3)
(4)
(5)
(6)
(7)
(8)
(9)
t (ms): 0
2.8
5.6
8.3
11.1
13.9
16.7
19.4
22.2
(10)
Bubble detachment (d_B=1.81 mm)
(11)
(12)
(13)
(14)
(15)
(16)
(17)
(18)
0.03 m
25
36.1
41.7
47.2
55.6
72.2
88.9
97.2
111.1

Figure 14